

The emergence of scale-free fires in Australia

Giorgio Nicoletti¹, Leonardo Saravia^{2,*}, Fernando Momo², Amos Maritan¹, Samir Suweis^{1,*}

¹*Laboratory of Interdisciplinary Physics, Department of Physics and Astronomy “Galileo Galilei”, University of Padova, Padova, Italy*

²*Área Biología y Bioinformática, Universidad Nacional de General Sarmiento, Buenos Aires, Argentina*

*Corresponding authors: lsaravia@campus.ungs.edu.ar; samir.suweis@unipd.it

Bushfires are an intrinsic part of Australia’s landscape, and its natural ecosystems have evolved to coexist with them¹. However, between 2019 and 2020, during the country’s hottest and driest year on record, Australia experienced a dramatic bushfire season, with catastrophic ecological and environmental consequences²⁻⁵. Several studies highlighted how such abrupt changes in fire regimes, in terms of size and spreading, may have been in large part a consequence of climate change and other anthropogenic transformations⁵⁻⁹. In this work, we analyze the monthly evolution of the burned area in Australia from 2000 to 2020, obtained via satellite imaging through the MODIS platform¹⁰. We find that the 2019-2020 peak of the burned area, the highest of the historical data, is associated with signatures that are typically found near tipping and critical points¹¹⁻¹³. We introduce a modeling framework based on forest-fire models^{14,15} to study these emergent fire outbreak properties, showing that the behavior observed during the 2019-2020 fire season matches the one of a percolation transition, where system-size outbreaks appear. Our model also highlights that a second type of critical point might be crossed, after which the vegetation cannot significantly recover anymore.

During the 2019-2020 fire season, around 5.8 million hectares of mainly temperate broadleaf forest were burned in New South Wales (NSW) and Victoria (VIC) in eastern Australia by a series of mega-fires. Many of the fires have exceeded 100,000ha and continued to burn for weeks after their ignition. Such mega-fires had a devastating impact on Australia biodiversity⁴: of more than 830 taxa, comprising birds, reptiles, frogs, mammals, and freshwater fish, around one third of them lost to the fires between 10% and 80% of the Australian extent of their habitat.

These drastic changes, with their catastrophic effects on the vegetation and on biodiversity, are often associated with tipping points, i.e. conditions that seem to inevitably lead to large-scale outbreaks and widespread damage^{13,16-18}. Such behavior has been observed in many different systems ranging from Amazon forests^{19,20} to Kalahari vegetation²¹ and more in general in tropical forests fragmentation^{22,23}. In physical systems with many degrees of freedom, these phenomena appear at critical points, where a phase transition occurs and scale-free behaviors characterized by power-laws emerge. In order to understand when and how these patterns emerged in Australia leading to the 2019-2020 bushfire season, we analyze a time-series of 236 monthly satellite images of Australia, spanning from November 2000 to June 2020. The exceptional nature of the 2019-2020 events is perhaps already striking from the time-series of the

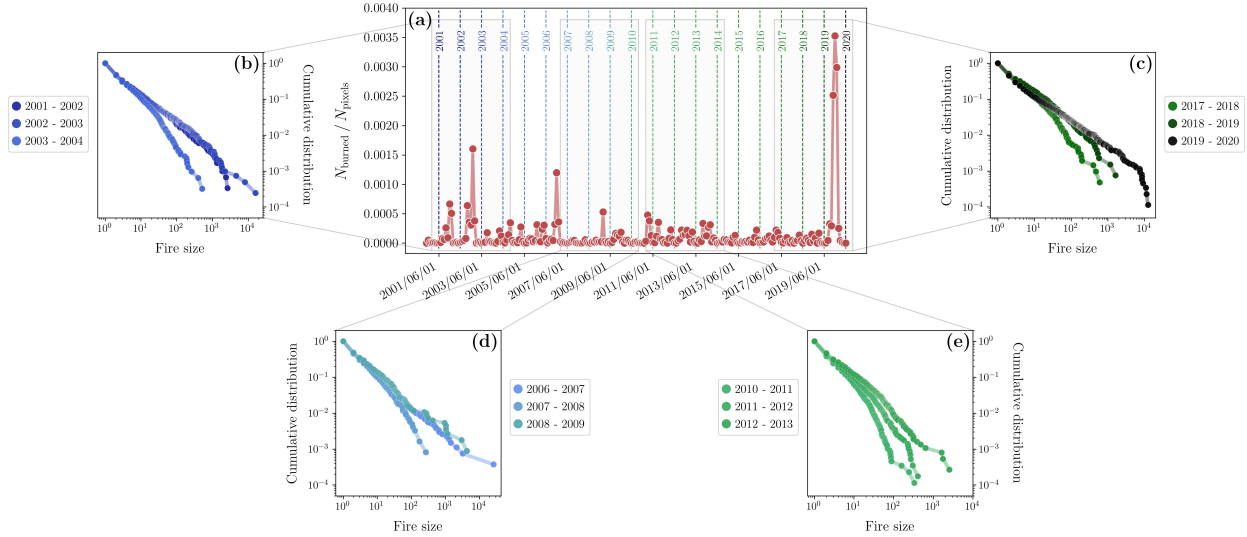


Figure 1: The cumulative distribution of the fire sizes at different years. (a) The time-series of the number of burned pixels per month in Australia, from 2000 to 2020. Years are defined as the twelve months occurring between June and May. The year 2019-2020 largely outmatched the peaks of the previous twenty years. (b-e) For a given year, we can compute the cumulative fire size distribution on a nearest-neighbor basis. Even though peaks, such as during 2002-2003, often display either longer tails in the distribution or are dominated by few, very large fires, a distinctive power-law behavior emerges during 2019-2020.

monthly burned area in the last 20 years (Figure 1a). As a gauge of the extent of the damage, less than half of the pixels were burning during the second largest peak - which took place in the season 2002-2003. Most importantly, given the spatial nature of our data, we can also compute the cumulative distribution of fire clusters' size on a nearest-neighbors basis (Methods) associated with a given year. These distributions (Figure 1b-e) typically display longer tails in concomitance of higher peaks of the burned area. However, during the 2019-2020 fire season such distribution becomes a consistent power-law over a wide range of sizes (Figure 1c). Crucially, such scale-free distribution might be tightly related to the dramatic impact that the 2019-2020 bushfire season had on the vegetation and on biodiversity. In fact, as few big fire clusters - corresponding to the distribution's long tails - devastated entire regions, in other areas smaller fires took place at the same time - the bulk of the power-law distribution - creating pockets of vegetation fuel that could act as an ignition to the next mega-fire. Such a catastrophic departure from the historical trend suggests that a fundamental shift in the underlying dynamics might have occurred.

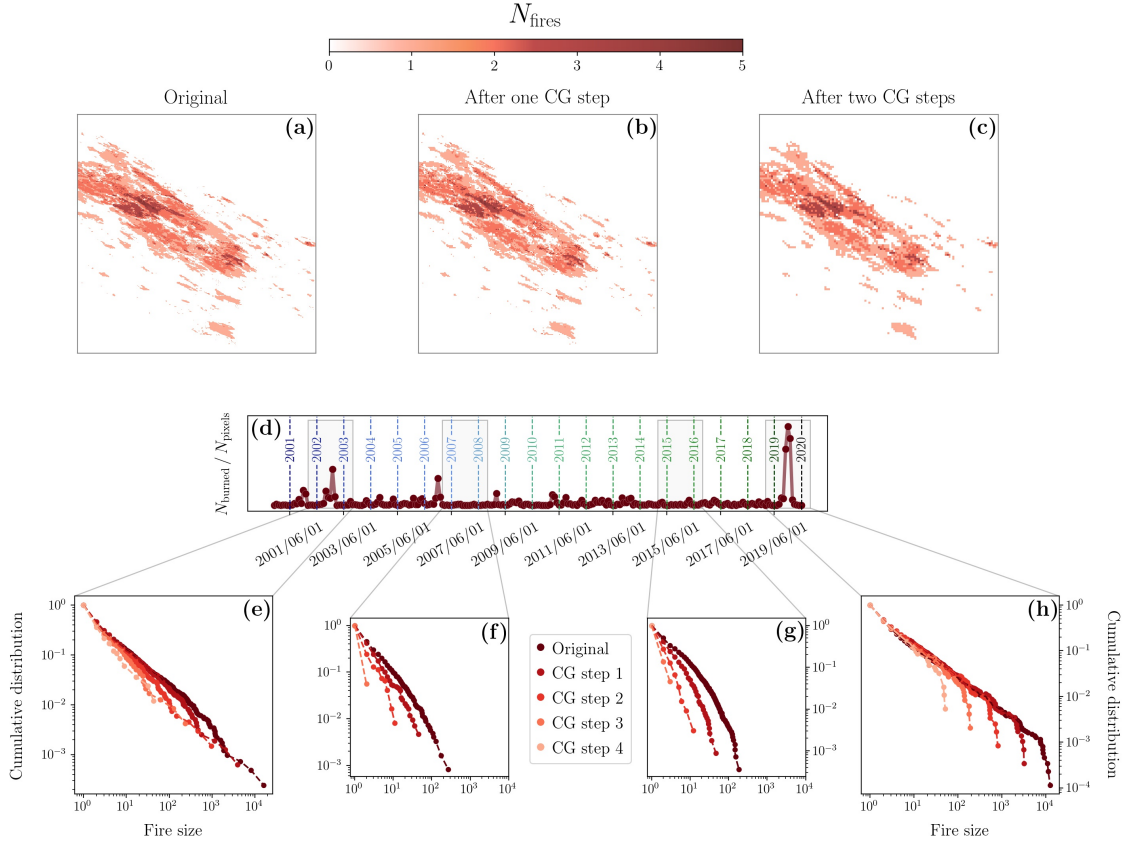


Figure 2: The properties of the data under spatial coarse-graining. (a-c) An example of three coarse-graining step of the overall number of fires per pixel during the 20 years present in our data. (d-h) The coarse-graining corroborates the presence of a very robust scale invariance during 2019-2020, whereas in the previous years the shape of the distribution is significantly changed by the CG transformation. For instance, during 2007-2008 and during 2015-2016 the distribution of the fire sizes is exponentially suppressed, and after four coarse-graining step there are almost no more fires to begin with.

Notably, some years (Figure 1d) show that larger fires than in 2019-2020 took place. In fact, a careful dynamical analysis of the time-series of number of fires per month, $N_{\text{fires}}(t)$, and of the size of the largest fire, $M_{\text{fires}}(t)$, show that during the 2019-2020 season Australia did not experience the largest fire in our data, nor the largest number of separated fire outbreaks. However, it is during 2019-2020 that a major synchronization between the two time-series emerges (see Methods section). These results suggest the dynamical presence of many and very large outbreaks at once, with a lack of a characteristic scale whose signature is the underlying power-law distribution.

Nevertheless, it is well-known that detecting power-law distributions in data is a non-trivial task²⁴⁻²⁶, nor there

is a one-to-one correspondence between power-laws and critical transitions. Therefore, we draw inspiration from one of the most powerful tools of Statistical Physics, the Renormalization Group^{11,27-29}. We perform, at each time, a spatial coarse-graining (CG) by grouping together nearby pixels through a majority rule (Methods) and we follow the fire-size distribution along these repeated transformations. A coarse-graining transformation amounts to study the system various spatial scales. If the system is truly scale invariant, its properties do not change under repeated CG transformations. Hence, and compatibly with the quality of the data, if the distribution of the fire size is a true power-law it will remain a power law after one or more CG transformations, with a corresponding finite-size scaling correction (Methods). In principle, one should iterate this transformation indefinitely to unravel the properties of its fixed points - however, with real data we are limited by the finite size of our system. After four CG steps, we are left with only $\approx 0.4\%$ of the initial number of pixels. If only few but large fires are present in the original system, this coarse-grained version will be dominated by system-sized outbreaks. On the other hand, if many but small fires characterized the initial state, the coarse-graining transformations will drive the system to a configuration where virtually no fires are present. In Figure 2a-e we plot the time-series of the monthly burned area for each CG step, renormalized by the total number of pixels that are present at that step, and we follow the cumulative distributions of the fire size along the coarse-graining³⁰. During the 2015-2016 season, for instance, the CG quickly suppresses the fire sizes distribution and only small fires are left. More interestingly, the distribution associated 2002-2003 season keeps its distinctive long tails along the coarse-graining, although the bulk of the distribution changes and no evident cut-off appears. However, it is during the 2019-2020 season that the power-law distribution of the fire size is left almost perfectly invariant, with a cut-off associated with the finite-size that scales accordingly. These results strongly suggest that, indeed, the power-law nature of the distribution is genuinely related to the underlying scale-invariance of the spatial structure of the fire outbreaks, which in turn manifest itself as a dynamical synchronization between the number of outbreaks and their maximum size. This results confirm that the emergent properties we observe are related to a phase transition. Thus, a fundamental question arises: what has driven 2019-2020 fire dynamics close to what appears to be a fully-fledged tipping point?

To answer this question we introduce a stochastic network forest-fire model that describes the concurrent

spreading of fires and of vegetation, as a function of few and environmentally relevant parameters. In Figure 3a-b we draw a pictorial depiction of the model as a multi-layer network³¹⁻³³ and of the corresponding rates. Without fires, the vegetation V is free to spread at a rate λ_V on a given graph - for instance, a 2-dimensional lattice - with death rate d_V , forming clusters of vegetation of size c_V . On top of this dynamics, a fire F can start on a vegetation site with rate b_F and spread with rate λ_F over an effective topology that is determined by the vegetation clusters. At the same time, the vegetation cannot occupy a site with a fire F , thus both the topology of the F layer and of the V layer will change dynamically with time. Once a fire is over, with a rate d_F , the corresponding site will become an empty site \emptyset for the vegetation layer, and will not be present in the fire layer.

For this model to be reasonable, we must assume that the vegetation dynamics is much slower than the one of the fires and that the birth rate of the fires b_F is typically very small (Figure 3c). With these assumptions, we look at how a fire propagates on top of a fixed stationary vegetation configuration, performing the simulation on a 2-dimensional lattice using a spatial version of the Gillespie algorithm³⁴. In this scenario, the model is described by the adimensional parameters $\zeta_F = d_F/\lambda_F$ and $\zeta_V = \lambda_V/d_V$ - a small value of ζ_F will give rise to fires that are extremely effective at spreading and, vice-versa, a large value of ζ_V implies a quick vegetation regrowth. Remarkably, since the vegetation layer in the absence of fires follows a simple contact process³⁵, we expect a percolation transition at $\zeta_V^{\text{perc}} \approx 2.6$, as recently shown³⁶. At this value, a system-size cluster of vegetation appears, coexisting with a significant number of distinct but smaller vegetation clusters (Figure 3d-e). This transition has a crucial impact on the cumulative distribution of the fire sizes s_F (Figure 3f-g). Below the percolation transition, fires are severely limited by the size of the vegetation clusters, and thus the distribution of s_F is exponentially suppressed. On the other hand, above the percolation threshold, the vegetation clusters tend to be much larger, and fires can be large provided that ζ_F is small enough.

Figure 4a shows the behavior of the ratio between the average fire size $\langle s_F \rangle$ and the average vegetation cluster size $\langle c_V \rangle$ in the parameter space (ζ_V, ζ_F) . This parameter is fundamental because it helps us understand the potentially damaging effects of the fires on the underlying vegetation substrate. Whenever $\langle s_F \rangle / \langle c_V \rangle \approx 1$, it implies that a fire

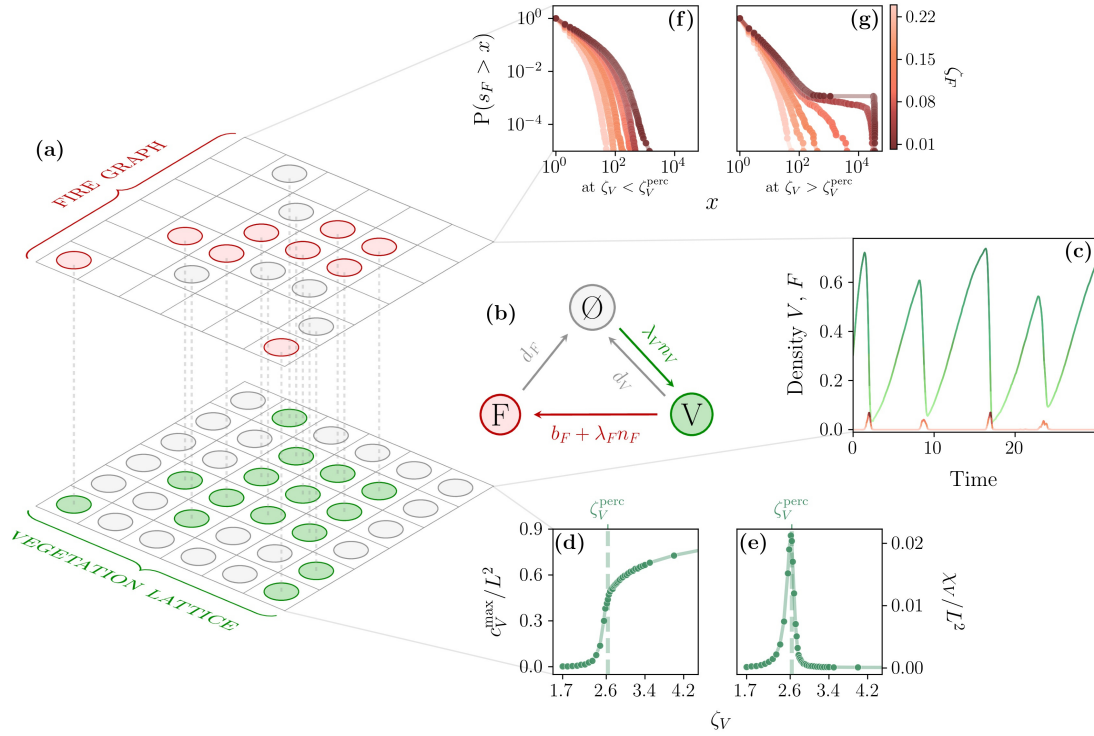


Figure 3: The fundamental properties of our model. (a-b) A pictorial depiction of the model dynamics as a multi-layer graph and the corresponding transition rates. (c) On a $2D$ lattice the model displays a charge-discharge behavior if the vegetation dynamics is much slower than the fires one, and fires are relatively rare events. Here $(d_F, b_F, \lambda_F) = (25, 10^{-5}, 500)$ and $(d_V, \lambda_V) = (0.5, 3)$. (d-e) The vegetation layer undergoes an isotropic percolation transition at $\zeta_V^{\text{perc}} \approx 2.63$ where a spanning cluster appears. In (d) we plot the size of the largest vegetation cluster c_V^{max} and in (e) the mean vegetation cluster size χ_V (as defined in Methods), which peaks at the transition. Both the plots are from a 250×250 lattice. (f) If consider fires that spread over a fixed vegetation configuration, below the percolation threshold ζ_V^{perc} (f) the cumulative distribution of the fire size s_F is always exponentially suppressed due to the small vegetation clusters. Above it (g), the fires may spread on a spanning cluster, and therefore we can have system-size outbreaks if ζ_F is small enough.

that originates in a given vegetation cluster has a non-vanishing probability to burn the entire cluster. The black dotted lines, instead, represent the contour lines of $\tilde{\chi} = s_F^{\text{max}} \times n_{c_V}$, where n_{c_V} is number of vegetation clusters. This quantity is particularly significant, because n_{c_V} can be interpreted as a rough estimate of the number of possible fires in the system, whereas s_F^{max} tells us how large they can be. In the data, these two quantities both reached high values at the same time during 2019-2020.

We find four different regimes, shown in Figure 4a-g. Whenever ζ_V is high enough, the system can quickly

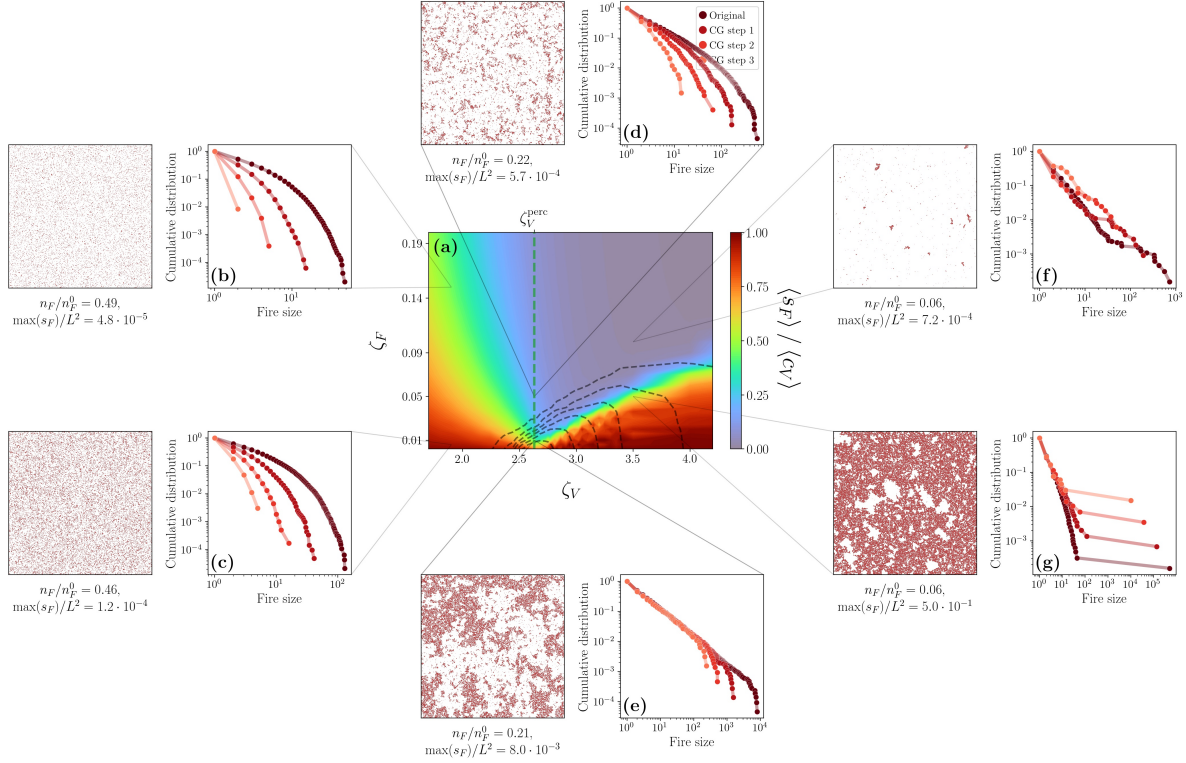


Figure 4: The properties of the time-scale separated model and its behavior under spatial coarse-graining. (a) At a given set of parameters (ζ_V , ζ_F) we plot the ratio between the mean fire size $\langle s_F \rangle$ and the mean size of a vegetation cluster $\langle c_V \rangle$ in a 250×250 lattice. The black dotted lines represent contour lines of $\bar{\chi}$, which is maximized around the percolation transition ζ_V^{perc} for low enough values of ζ_F . (b-g) We simulate $n_F^0 = 10^5$ fires on a lattice with linear size $L = 1000$ in order to study the distribution of the fire sizes s_F and the corresponding coarse-grained distributions. (b-c) At low values of ζ_V the cumulative distribution of the fire sizes is exponential and is further suppressed along the coarse-graining at all values of ζ_F . (d-e) At ζ_V^{perc} , if ζ_F is low enough the fire size distribution becomes a power-law that is invariant along the coarse-graining. (f-g) For high values of ζ_V , on the other hand, the system is dominated by few large clusters of vegetation, and the corresponding large fires are highlighted by the coarse-graining. This regime is not particularly realistic at low ζ_F , since it would require climate conditions that allow for large fires, i.e., a warm and arid climate, but at the same time for an extremely effective vegetation spread.

spread any burned vegetation. If also ζ_F is high, fires are small and the system is dominated by large vegetation clusters, giving rise to a vegetation-rich regime where we expect to see a small burned area (Figure 4d). If, instead, ζ_F is low, fires can propagate almost unboundedly due to the underlying large vegetation clusters (Figure 4e). This regime is perhaps unrealistic, but it could be observed in fire-prone communities where species with post-fire recruitment have the most flammable canopies³⁷. On the other hand, if ζ_V is low, the vegetation regrowth is typically suppressed. In this case, when ζ_F is high, fires tend to be small (Figure 4b), but so do the clusters of vegetation. Indeed, $\langle s_F \rangle / \langle c_V \rangle$ can

dangerously increase because substantial parts of the underlying vegetation clusters can burn even at high ζ_F . Finally, when ζ_F is also low, not only the vegetation clusters can hardly regrow, but a fire can systematically burn the entire cluster in which it originates since $\langle s_F \rangle / \langle c_V \rangle \approx 1$. This regime is not sustainable in the long time - the fires are likely to outpace the vegetation regrowth and eventually the system slowly dies. Moreover, it cannot be detected from the distribution of the fire sizes, in Figure 4c, which stays exponential.

The vegetation percolation transition lies in between these regimes, and it is here that power-law distributed fires emerge at low enough ζ_F (Figure 4f-g). Although $\langle s_F \rangle / \langle c_V \rangle$ remains small in this regime due to the fact that the mean itself is not representative of scale-free phenomena, we clearly see a distinctive scale-invariant configuration emerging, with a power-law distribution that is left almost untouched by the spatial coarse-graining. Moreover, this is also the region where $\max s_F \times n_{c_V}$ is maximized, since the system can experience both large and small fires at the same time. All in all, it is at this critical point that our model describes best the features that we see during the 2019-2020 fire season.

How did Australia reach such a tipping point? Realistically, we expect the control parameters ζ_V and ζ_F to be determined by the climate conditions. A changing climate with prolonged droughts, higher temperatures, and a more arid climate - recognized as propelling events that lead to the 2019-2020 bushfire season^{6,9} - might have pushed both ζ_V and ζ_F to lower and lower values, eventually reaching and crossing the percolation transition between 2019 and 2020. In fact, the 2019-2020 year has been unusually hot and dry in part due to natural meteorological phenomena, such as a shift in the polar winds above Antarctica and one of the strongest positive swings in the Indian Ocean Dipole. The former contributed to stratospheric warming, which in turn contributed to bringing hot, dry weather to much of Australia. The latter, in its positive phase, can lead to a reduction in rainfall over the southern and most northerly regions of Australia⁶. However, on top of - and possibly as a cause of - all this natural variation, global warming is making the country even hotter and drier³⁸, with the devastating effects that we highlighted in the previous sections of this work.

Finally, our paradigmatic model predicts the presence of yet another critical point, one of a very different

nature associated with the absorbing phase transition of the contact process at $\lambda_V/d_V := \zeta_V^{\text{abs}} \approx 1.6^{35}$. Indeed, once the vegetation spreading is slowed down enough, not only fires can have a devastating effect even at high values of ζ_F , but the vegetation is doomed to never recover. However, one should consider that broadleaf Australian forest species, such as Eucalyptus, have resilience and resistance traits, like resprouting and seed banks, that allow for a rapid post-fire recovering even in intense fire-regimes^{39,40}. Still, repeated fires with short return times would cause the exhaustion of these capacities⁴¹ and eventually, beyond the absorbing phase transition at $\zeta_V < \zeta_V^{\text{abs}}$, the model predicts a completely empty configuration where the fires have burned the vegetation to extinction. While this critical point is probably too simple to describe the highly complex dynamics that determines the spreading of real fires, it does suggest that the isotropic percolation transition observed during the 2019-2020 bushfire crisis may foreshadow a worsening condition that might lead in the far future to a forest-savanna-like type of transition^{42,43}.

Our results show that the presence of scale-free outbreaks during the 2019-2020 bushfire seasons is connected to environmental and ecological drivers of both fires and vegetation dynamics, and suggest that Australia might be close to critical transition. Future works should focus on developing quantitative methods to measure from data the contributions of natural variations and of the anthropogenic impact on the parameters of complex models, where both fires and vegetation evolve and spread, and to assess from them mitigation strategies that are more and more vital. It is very probable, if not unavoidable, that worsening environmental and climate conditions will bring more forest ecosystems close to these tipping points⁴⁴, increasing the risk of drastic, devastating and unprecedented changes.

Acknowledgments. AM is supported by “Excellence Project 2018” of the Cariparo foundation.

Author contributions. LS and SS designed the study. LS, AM, SS supervised the research. LS and FM collected the data. GN analyzed the data. GN, AM and SS designed and studied the model. GN performed the simulations. GN, LS, AM and SS interpreted the results and wrote the manuscripts. All authors contributed to the article and approved the submitted version.

METHODS

Data collection. We defined the region of study as the East and Southeast temperate broadleaf and mixed forests of continental Australia using the ecoregions defined by Dinerstein⁴⁵, accessible at <http://ecoregions2017.appspot.com/>, which represents an area of 48e06 ha (Figure of study region). For this region we estimate the burned areas using the NASA Moderate-Resolution Imaging Spectroradiometer (MODIS) burnt area Collection 6 product MCD64A1¹⁰, which is a monthly product with a 500 m pixel resolution. We downloaded the images, using Google Earth Engine, as geoTIFF and then we converted them to a binary matrix (circa 4000x8000) using the R statistical language⁴⁶. Then, for each month we have a binary matrix M_t , whose pixel represent an area of 500 m² and can be either 1 - if there has been a fire in that pixel in the span of that month - or 0 - if no event occurred, meaning that no burned area was detected.

Cluster distribution. We define a cluster of a binary matrix M_t using a nearest-neighbors connectivity, i.e. the pixels that belong to a cluster are defined using the connectivity matrix

$$C_{\text{basis}} = \begin{pmatrix} 0 & 1 & 0 \\ 1 & 1 & 1 \\ 0 & 1 & 0 \end{pmatrix}$$

which defines the usual nearest neighbors of a 2-dimensional lattice. We also repeated the analysis described in the main text using a next-nearest-neighbors connectivity and the results do not change significantly. Therefore, for each matrix M_t we end up with a number of clusters $n_c(t)$ and a the areas of each cluster $\{A_c^{(i)}\}_{i=1}^{n_c(t)}$. Then the cumulative fire size distribution of M_t can simply be evaluated as

$$P(s_F) := P(A_c > s_F) = \sum_{i=1}^{n_c(t)} \frac{\theta(A_c^{(i)} - s_F)}{\sum_i A_c^{(i)}}$$

where $\theta(\cdot)$ is the Heaviside function.

Cluster dynamics. Since both the number of clusters and their areas are a function of time, we can exploit their time-series to learn something about the underlying properties of the fire dynamics. In particular, we look at the number



Figure M1: The shaded area represents the region of study encompassing the East and Southeast temperate broadleaf and mixed forests of continental Australia.

of clusters $n_c(t) = N_{\text{fires}}(t)$ and the area of the largest cluster $m_c(t) = \max_i \{A_c^{(i)}\}_{i=1}^{n_c(t)} = M_{\text{fires}}(t)$. We normalize both these time-series by dividing them by their maximum value, in order to make them comparable, and we plot them in Figure M2c. Notice that other normalizations, such as a standard z-score, give essentially the same results as one reasonably expects. In order to understand how the evolution of these two time-series relates in time, we need to introduce their Hilbert transform. In general, the Hilbert transform of a real-valued time-series $x(t)$ is defined as

$$\mathcal{H}[x(t)] = x(t) + \frac{i}{\pi} \lim_{\varepsilon \rightarrow 0} \int_{\varepsilon}^{\infty} \frac{x(t + \tau) - x(t - \tau)}{\tau} d\tau$$

which is a complex number. Thus we can look at its phase

$$\varphi_x(t) = \arctan \frac{\text{Im}[\mathcal{H}[x(t)]]}{\text{Re}[\mathcal{H}[x(t)]]}$$

and its modulus

$$\rho_x(t) = \sqrt{\text{Im}^2[\mathcal{H}[x(t)]] + \text{Re}^2[\mathcal{H}[x(t)]]}$$

and how they change in time in Figure M2a-b. In general, we do not expect these time-series to be in sync and indeed we typically see that finding a high number of clusters usually does not imply having large clusters as well. There are a few notable exceptions, as noted in the main text, in particular during 2019-2020. Remarkably, neither the modulus of $\mathcal{H}[N_{\text{fires}}(t)]$ nor the one of $\mathcal{H}[M_{\text{fires}}(t)]$ are the largest during the months of 2019-2020, but they both

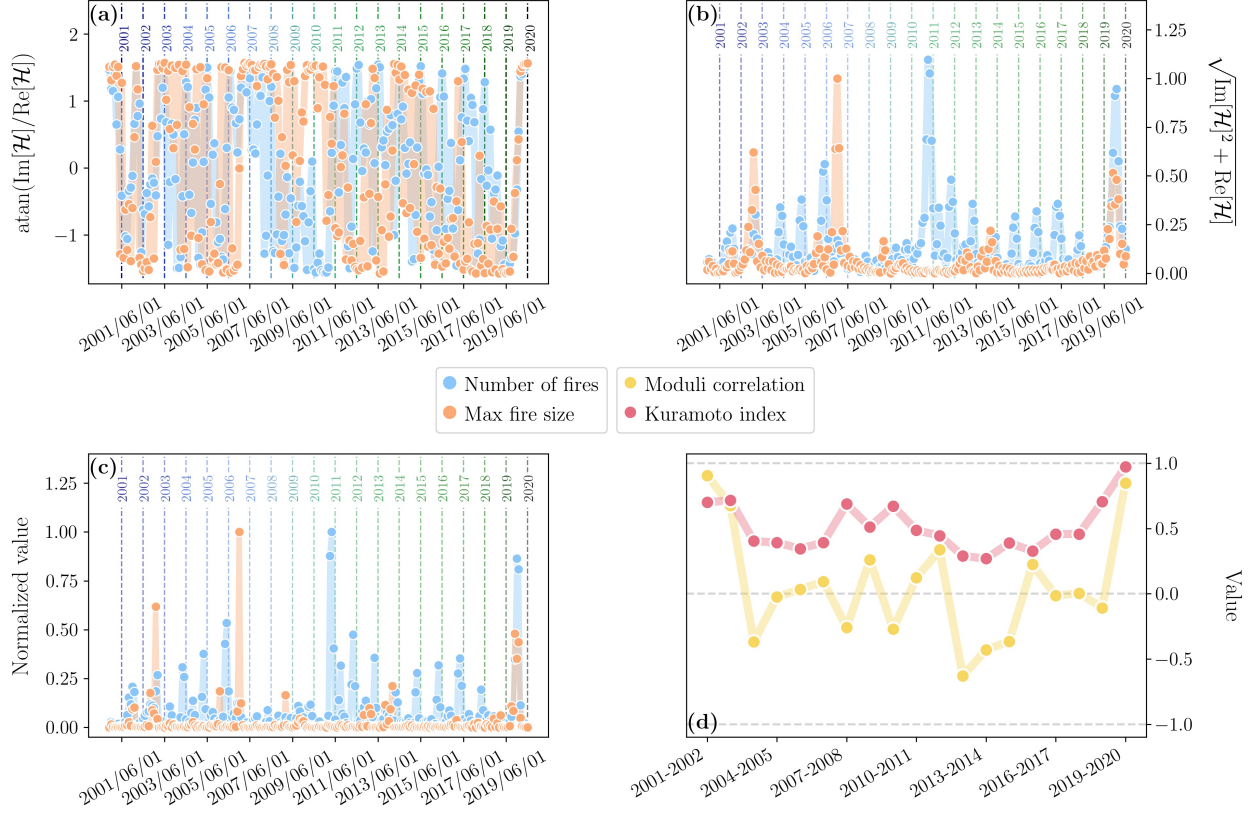


Figure M2: (a) The phase of the Hilbert transform of both the time-series of the number of fires and of the maximum fire size show a major synchronization during 2019-2020. (b) Similarly, the corresponding amplitudes suggest that during the 2019-2020 fire season a very large number of fires coexisted together with extremely large ones. This behavior is indeed captured by the power-law behavior of the fire size distribution. (c) Plot of $N_{\text{fires}}(t)$, the number of fire outbreaks in a given month, and of $M_{\text{fires}}(t)$, the largest outbreak of a given month. Both timeseries have been normalized by their maximum value in order to compare them. (d) The Kuramoto index between the phases of the Hilbert transform of $n_c(t)$ and of $m_c(t)$ and the correlation between the respective moduli. A clear synchronization emerges during 2019-2020, and in the same year the correlation between the moduli spikes as well. This behavior is of course compatible with the power-law cumulative distribution of the fire sizes that is found in the same year.

attain higher-than-average values leading to the coexistence of many small fires and few exceptionally large ones.

We can further quantify the relations between $n_c(t)$ and $m_c(t)$ by looking at the Kuramoto index⁴⁷ of their Hilbert transforms and at the correlation between the corresponding moduli. We define the Kuramoto index on a given

year as

$$K_{\text{year}} = \left| \left\langle e^{\varphi_{n_c}(t) - \varphi_{m_c}(t)} \right\rangle_{\text{year}} \right|$$

and the correlation between the moduli as

$$C_{\text{year}} = \frac{\langle \rho_{n_c} \rho_{m_c} \rangle_{\text{year}} - \langle \rho_{n_c} \rangle_{\text{year}} \langle \rho_{m_c} \rangle_{\text{year}}}{\sqrt{\prod_{i \in \{m_c, n_c\}} [\langle \rho_i^2 \rangle_{\text{year}} - \langle \rho_i \rangle_{\text{year}}^2]}}.$$

In Figure M2d we do indeed see that K_{year} becomes significantly close to 1 during 2019-2020, hence the two time-series are almost perfectly synchronized during the year. Similarly, the correlation between the moduli has a positive spike in the same period. It is worth noting that this is true even if in the original time-series neither the number of clusters nor the size of the largest one are maximal during 2019-2020. The fundamental change in the behavior of the system is that during this year *both* of them peak in a synchronized fashion, which leads to the power-law distribution that we have shown in the main text.

Spatial coarse-graining. A quantitative and powerful way to assess the scale-invariance of a system is given by a properly defined coarse-graining procedure^{11,27,29}. In the spirit of Statistical Physics, a suitable coarse-graining for a binary matrix M_t is a block-spin transformation of the associated 2-dimensional square lattice. Namely, the k -th coarse-graining step amounts to define a super-pixel $\sigma_{i'}^{(k+1)}$ from the previous pixels $\sigma_i^{(k)}$ via the majority rule

$$\sigma_{i'}^{(k+1)} = \begin{cases} 1 & \text{if } \sum_{j \in B_i} \sigma_j^{(k)} > \lfloor \text{card}(B_i)/2 \rfloor \\ 0 & \text{otherwise} \end{cases}$$

where $\lfloor \cdot \rfloor$ is the floor function and B_i is the i -th set of pixels such that $\{B_i\}$ forms a non-overlapping covering the original 2-dimensional lattice. In particular, we take $B_i \in \mathbb{M}(2 \times 2)$ so that at each coarse-graining step the number of pixels is reduced to a fourth of the original ones and therefore we can perform enough coarse-graining steps. Notice that in this case the majority rule is not exact since the cardinality of B_i is even. Thus, if $\sum_{j \in B_i} s_j^{(k)} = 2$ we randomly assign the value of $s_{i'}^{(k+1)}$ to be either 0 or 1.

In the spirit of the Renormalization Group, we should follow physical observables and - in particular - probability distributions³⁰ to look for scale-invariance along the coarse-graining. That is, if the system is scale-invariant in

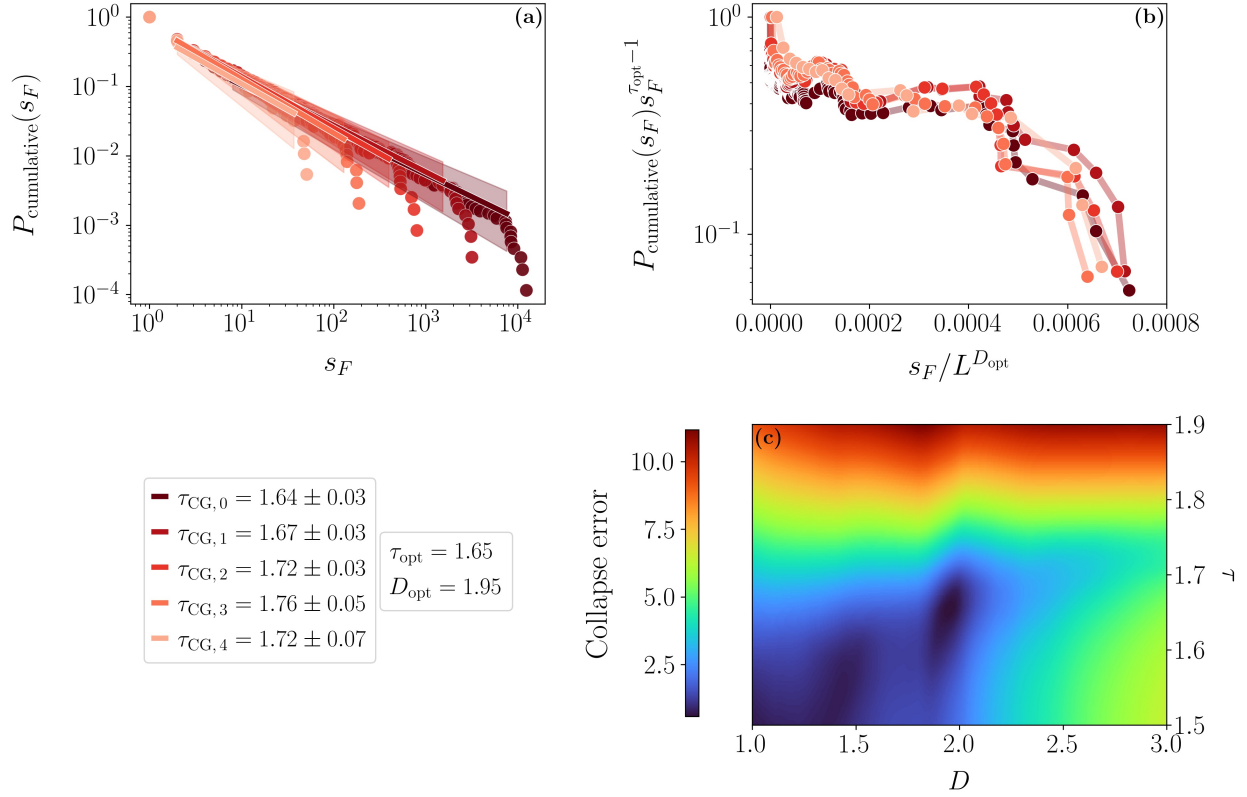


Figure M3: (a) The cumulative distribution of the fire sizes during 2019-2020 along the coarse-graining transformations, with the best power-law fit obtained minimizing the Kolmogorov-Smirnov distance²⁴. Notice how the exponents of the power-laws remain compatible at different CG steps. Notice that the different τ reported here are already the exponents of the fire size distribution, not of the cumulative distribution. (b) The cumulative distributions of the data at different CG steps collapse into the same curve, once appropriately rescaled, as predicted by finite-size scaling. In order to appreciate the quality of the collapse, notice the different units in the vertical axis with respect to panel (a). (c) The two parameters τ and D that are needed to collapse the cumulative distributions of the fire sizes can be chosen so that the collapse error will be minimal⁴⁸. As expected, we find $\tau_{\text{opt}} \approx 1.65$, which is compatible with the fitted exponent.

a spatial sense we should see that, even if we are coarse-graining the system, some of its properties will not change up to some finite-size cutoff, because the small-scale features are indistinguishable from the large-scale ones. This is exactly what we look for when we compare the cumulative probability distributions of the cluster sizes at different coarse-graining steps.

As at each coarse-graining step we observe a smaller and smaller system, we can exploit finite-size scaling. Thinking of a percolation-like transition⁴⁹, the probability distribution of the fire sizes in a system of linear size L

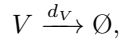
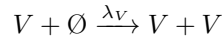
scales as

$$P_{\text{cumulative}}(s_F) = s_F^{-\tau+1} \psi\left(\frac{s_F}{L^D}\right)$$

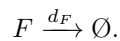
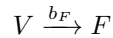
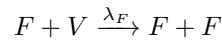
where D is related to the critical exponent of the correlation length and τ is the exponent of the power-law distributed fire sizes. In particular, D is the fractal dimension of the fires. Hence, for a properly chosen value of D , we expect that $P_{\text{cumulative}}(s_F)s_F^{\tau-1}$ as a function of s_F/L^D will collapse onto the same curve. In Figure M3 we show that indeed we find this collapse with $D \approx 1.95$, which suggests once more, and in terms of the Renormalization Group, that the 2019-2020 fire seasons appears to behave like a system close to a phase transition. In fact, the fractal dimension tells us the size s_F of a fire outbreak changes with its linear size, i.e., $s_F \sim L^D$.

The model. The phase transition that is suggested by the data is not trivial, because it involves scale-invariant spatial features, synchronization in the cluster dynamics, and possibly a percolation-like behavior in space. Moreover, we typically think of spreading models as models with an absorbing phase transition, i.e. a directed percolation transition, such as the contact process³⁵. This transition is not necessarily the one suggested by the data, where fires appear at all scales, similarly to what happens in isotropic percolation.

As a general scheme, we can build a three-state model as in Figure 3b. Each site can be either in an empty state \emptyset , in a vegetation state V or in a fire state F . Then we have the following reactions for the vegetation sector of the model



and the following reactions for the fire sector



As we can see, the first reactions are symmetric under the transformation ($V \rightarrow F, \emptyset \rightarrow V$) but this symmetry is

broken in particular by the last reaction, which represents the death of a fire. Indeed, the vegetation sector of the model, if considered independently, is a standard contact process with death rate d_V and spreading rate λ_V ; the fire sector, if considered independently, represents instead a contact process with birth rate b_F , death rate d_F and spreading rate λ_F , with the additional property of resource depletion - meaning that the dead sites become unavailable. Thus, there is an intrinsic difference in the two sectors due to the structure of the reactions.

Since the vegetation can only spread through nearest neighbors, the contact process of the vegetation displays both an absorbing phase transition - so that it can effectively go extinct - and a percolation transition³⁶. Even so, in the coupled model the picture is particularly complex. The fires spread over the effective topology determined by the vegetation patterns, so the topology for the fire contact process is not constant in time. Similarly, due to the presence of fires, the topology over which V can spread will change dynamically as well due to the presence of F sites that are unavailable for the vegetation. It is easy to imagine that in such a scenario the actual underlying topology will matter greatly: we expect that a 2-dimensional lattice will give very different results with respect to, say, a fully connected model.

At $\zeta_V = \zeta_V^{\text{perc}}$, in particular, if $L \rightarrow \infty$ an infinite cluster of vegetation appears. If we call c_V the vegetation cluster size and $n(c_V)$ the number of vegetation clusters of size c_V , we can define the mean vegetation cluster size⁴⁹ as

$$\chi_V = \frac{\sum_{c_V} (c_V)^2 n(c_V)}{\sum_{c_V} c_V n(c_V)}$$

where the sum runs over all vegetation clusters. This quantity, which we plot in Figure 3e, is expected to diverge at the percolation transition. Notice also that in bond percolation we would expect the fractal dimension to be $D = 91/48 \approx 1.896$ in a two-dimensional lattice, which is compatible from what we find in data. However, the exponent τ of the fire size distribution is different from the one expected in bond percolation, suggesting that the universality class might be different. Let us note that, in our model, bond percolation only happens in the isolated vegetation layer, and not in the fires one.

Mean-field behavior of the model. The MF equations read

$$\begin{aligned}\frac{dp_{\emptyset}}{dt} &= -\lambda_V p_V p_{\emptyset} + d_F p_F + d_V p_V \\ \frac{dp_F}{dt} &= -d_F p_F + (\lambda_F p_F + b_F) p_V \\ \frac{dp_V}{dt} &= -(d_V + b_F + \lambda_F p_F) p_V + \lambda_V p_V p_{\emptyset}\end{aligned}$$

where p_{\emptyset} , p_F and p_V are the probabilities of each state. Since $p_{\emptyset} = 1 - p_F - p_V$ we consider only the equations for p_F and p_V . In general, the stationary state of the system is given by

$$\begin{cases} d_F p_F = (\lambda_F p_F + b_F) p_V \\ (d_V + b_F + \lambda_F p_F) p_V = \lambda_V p_V (1 - p_V - p_F) \end{cases}$$

These equation have an absorbing configuration as a solution, since $(p_V^{\text{abs}}, p_F^{\text{abs}}) = (0, 0)$ is a trivial solution of the system. The Jacobian matrix evaluated at $(p_V^{\text{abs}}, p_F^{\text{abs}})$ is given by

$$J^{\text{abs}} = \begin{pmatrix} -d_F & b_F \\ 0 & -(b_F + d_V) + \lambda_V \end{pmatrix}$$

whose eigenvalues are $\mu_1^{\text{abs}} = -d_F$ and $\mu_2^{\text{abs}} = \lambda_V - b_F - d_V$. Thus, the empty state is only stable below $\lambda_V^{\text{abs}} = b_F + d_V$, which is the absorbing critical point of the system. Notice that λ_F does not play a meaningful role in the stability of the empty state, a feature that is likely wrong in a spatially embedded model.

The other stationary state of the system is given by

$$\begin{aligned}p_F^{\text{stat}} &= \frac{-d_V \lambda_F - (b_F + d_F + \lambda_F) \lambda_V + \sqrt{f_{F,V}^{\text{stat}}}}{2\lambda_F \lambda_V} \\ p_V^{\text{stat}} &= \frac{\lambda_F (-2b_F - d_V) - (b_F + d_F - \lambda_F) \lambda_V + \sqrt{f_{F,V}^{\text{stat}}}}{2\lambda_F (\lambda_F + \lambda_V)}\end{aligned}$$

where

$$f_{F,V}^{\text{stat}} = 4d_F \lambda_V \lambda_F (\lambda_V^{\text{abs}} - \lambda_V) + (d_V \lambda_F - (b_F + d_F + \lambda_F) \lambda_V)^2$$

is positive above λ_V^{abs} . While the eigenvalues of J^{st} are quite complicated, they always have a negative real part if $\lambda_V > b_F + d_V$ while they always may have a non-vanishing imaginary part. Hence, the relaxation towards the steady-state typically happens in an oscillatory fashion. In particular, these oscillations play a major role in the evolution

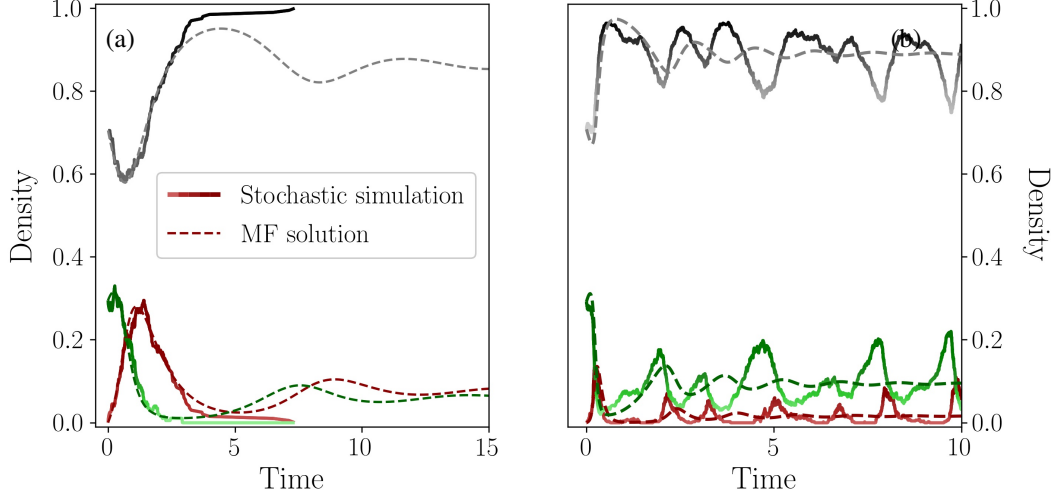


Figure M4: Comparison between the analytic solution of the deterministic mean field equations and a trajectory of the stochastic simulation on a fully connected networks with 500 nodes. (a) With parameters $(d_F, b_F, \lambda_F) = (1, 0.5, 10)$ and $(d_V, \lambda_V) = (0.01, 1.5)$ the absorbing state is unstable, and indeed the stationary solution of the mean field converges to the expected values $(p_O^{\text{stat}}, p_F^{\text{stat}}, p_V^{\text{stat}})$. However, due to the fact that the initial transient drives the system close to the absorbing state, the finite size of the system makes it possible for the noise to push the system to a completely empty configuration. (b) For $(d_F, b_F, \lambda_F) = (10, 0.1, 100)$ and $(d_V, \lambda_V) = (1, 3)$, instead, the system never reaches the absorbing state but sustained oscillations around the stationary values $(p_O^{\text{stat}}, p_F^{\text{stat}}, p_V^{\text{stat}})$ emerge after an initial transient.

of the finite-size stochastic model, where the noise can push the system to the absorbing state or produce sustained stochastic oscillations, as we see in Figure M4.

In general, we expect the mean-field picture to be drastically different from a spatially embedded model. Indeed, the spatial structure significantly changes the way fires can spread due to the underlying vegetation structure, as explained in the main text, and it introduces the notion of isotropic percolation which is the main mechanism behind the transition we studied in this work.

Exact stochastic simulation. Simulations of the three-state model on a given network, such as a 2-dimensional lattice, are performed using a generalized version of the Gillespie algorithm³⁴. Suppose that there are N sites in the network and that there are M possible transitions - in our model, $M = 6$. Then, at each time the network can be associated with a propensity matrix $A_{\mu i}^{(t)}$, where $\mu = 1, \dots, N$ and $i = 1, \dots, M$. Each row of $A_{\mu i}^{(t)}$ is given by the transition

rates that the μ -th site can undergo, given its state at time t . We introduce the total propensity $\alpha_0^{(t)} = \sum_{\mu} \sum_i A_{\mu i}^{(t)}$, so that the waiting time for the next transition is given by

$$\tau^{(t)} = -(\alpha_0^{(t)})^{-1} \log u$$

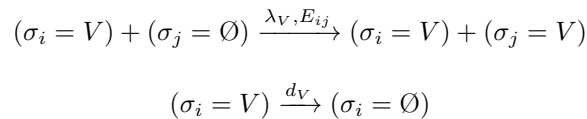
where u is uniformly distributed in $[0, 1]$. Then, the transition \bar{i} that occurs and the site $\bar{\mu}$ at which it occurs are such that

$$\sum_{\mu=1}^{\bar{\mu}-1} \sum_{i=1}^{\bar{i}-1} A_{\mu i}^{(t)} \leq \alpha_0^{(t)} v < \sum_{\mu=1}^{\bar{\mu}} \sum_{i=1}^{\bar{i}} A_{\mu i}^{(t)}$$

where v is once again uniformly distributed in $[0, 1]$. We then update $A_{\bar{\mu} \bar{i}}$ with the new transition rates for $\bar{\mu}$ and set the time to $t + \tau$.

Explicit time-scale separation. As pointed out in the main text, it is reasonable to expect that the vegetation dynamics is much slower than the fire dynamics. However, the parameter space of the model is extremely large and thus a phase space plot for the full model proves to be unfeasible. Therefore, in order to simplify the problem and reduce the number of free parameters, we can assume that the vegetation configuration does not change during the propagation of a fire. This approximation is compatible with the time evolution of the model if we also assume that fires are rare events and thus we end up with a charge-discharge dynamics and indeed it is well justified by the fact that the complete model does indeed follow a charge-discharge dynamics, with periods of almost undisturbed vegetation spreading followed by faster periods of fire spreading. In fact, realistically, we expect the vegetation - if dry enough - to act as fuel during a fire propagation, which thus has to stop when locally all fuel is exhausted. Then the vegetation regrows and only after enough fuel is accumulated a new fire can start - that is, the two processes are reasonably separated in their timescales.

Let us start with a network $(\{\sigma_i\}_{i=1}^N, \{E_{ij}\})$ where the N sites σ_i are such that $\sigma_i \in \{\emptyset, V\}$ and $\{E_{ij}\}$ are the edges between the sites. We look for a stationary configuration $\{\sigma_i^{\text{stat}}\}_{i=1}^N$ of the reactions



where the notation $\xrightarrow{\lambda_V, E_{ij}}$ means that the reaction happens at a rate λ_V if and only if i and j are joined by an edge

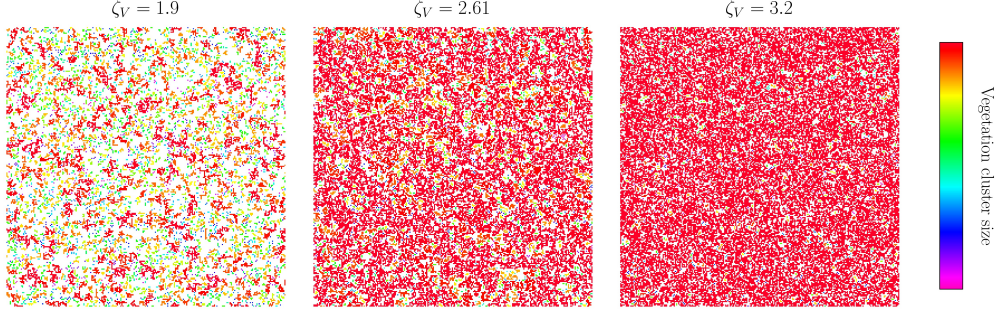
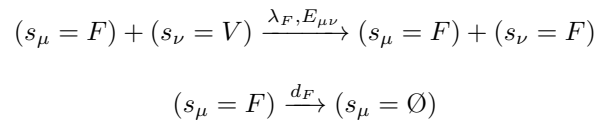


Figure M5: Three stationary configurations of the vegetation contact process at different values of ζ_V in a 250×250 2-dimensional lattice. Different colors represent clusters of different sizes. Notice how at the percolation threshold a system-size cluster appears.

E_{ij} . The system has an absorbing configuration $\{\sigma_i = \emptyset\}$ and its stationary configurations only depend on the ratio of the reaction rates $\zeta_V = \lambda_V/d_V$. In Figure M5 we show three examples of such configurations in a 2-dimensional lattice.

Our approximation consists in using the stationary configuration $\{\sigma_i^{\text{stat}}\}_{i=1}^N$ to obtain a (fixed) network over which the fires can spread. In particular, we consider the subgraph induced by the map $g : i \mapsto \mu$ defined for all the indexes i such that $\sigma_i = V$. If we call these sites $s_\mu = \sigma_{g(i)}$, we end up with the vegetation subgraph $(\{s_\mu\}_{\mu=1}^{N_V}, \{E_{\mu\nu}\})$ where $E_{\mu\nu} = E_{g(i)g(j)}$ and N_V is the number of original vegetation sites. This subgraph is typically composed of many disjointed components. These components contain roughly the same number of nodes for $\zeta_V^{\text{abs}} < \zeta_V \ll \zeta_V^{\text{perc}}$, since the stationary configuration is dominated by a large number of small vegetation clusters, whereas as we approach ζ_V^{perc} a giant component emerges and it is eventually dominant for $\zeta_V \gg \zeta_V^{\text{perc}}$.

We now assume that $s_\mu \in \{\emptyset, V, F\}$, and notice that the initial configuration is such that $s_\mu = V, \forall \mu = 1, \dots, N_V$. In order to sample the distribution of the fire sizes we can choose a site $s_{\bar{\mu}}$ and set $s_{\bar{\mu}} = F$. Then, we let the following reactions take place



until there are no more F sites in the network. Thus, the fire dynamics only depend on $\zeta_F = d_F/\lambda_F$. The fire size is

then simply given by the number of empty sites N_{\emptyset} of the final configuration.

One should be careful that if $s_{\bar{\mu}}$ is chosen at random between all sites we typically favor larger components of the vegetation subgraph. Thus, we first uniformly sample a given component C_s of the vegetation subgraph, and then we randomly choose a site within such component and set $C_s \ni s_{\bar{\mu}} = F$. Notice that this assumption is qualitatively equivalent to the assumption that if two fires start in the same cluster they will contribute to the same burned area. To be precise, this is only true if ζ_F is small enough, so that two fires inside the same component will meet each other with high probability. However, for larger values of ζ_F we expect fires to be small no matter what, thus they will hardly be affected by the size of the underlying component. In this way, we are now able to computationally explore the model's behavior effectively and systematically. In particular, our aim is to understand the different regimes that emerge in different regions of the parameter space (ζ_V, ζ_F) and to assess their quantitative properties in terms of the distribution of s_F and its behavior under a spatial CG, in order to gain an intuition on the mechanism that underlies the 2019-2020 outbreaks. Hence, for each value of ζ_V , we simulate a large number of stationary configurations $\{\sigma_i^{\text{stat}}\}_{i=1}^N$. Then, for each of these configurations, at a given value ζ_F we simulate a number of fires much larger than the number of components C_s , thus ending up with a set of burned areas $\{N_{\emptyset}\}$ that gives us the fire size distribution at (ζ_F, ζ_V) .

1. Yates, C. P., Edwards, A. C. & Russell-Smith, J. Big fires and their ecological impacts in australian savannas: size and frequency matters. *International Journal of Wildland Fire* **17**, 768–781 (2008).
2. Lindenmayer, D. B. & Taylor, C. New spatial analyses of australian wildfires highlight the need for new fire, resource, and conservation policies. *Proceedings of the National Academy of Sciences* **117**, 12481–12485 (2020).
3. Deb, P. *et al.* Causes of the widespread 2019–2020 australian bushfire season. *Earth's Future* **8**, e2020EF001671 (2020).
4. Ward, M. *et al.* Impact of 2019–2020 mega-fires on australian fauna habitat. *Nature Ecology & Evolution* **4**, 1321–1326 (2020).
5. Phillips, N. & Nogrady, B. The race to decipher how climate change influenced australia's record fires. *Nature* **577**, 610–613 (2020).
6. Dowdy, A. J. Climatological variability of fire weather in australia. *Journal of Applied Meteorology and Climatology* **57**, 221–234 (2018).
7. Yu, P., Xu, R., Abramson, M. J., Li, S. & Guo, Y. Bushfires in australia: a serious health emergency under climate change. *The Lancet Planetary Health* **4**, e7–e8 (2020).
8. Boer, M. M., de Dios, V. R. & Bradstock, R. A. Unprecedented burn area of australian mega forest fires. *Nature Climate Change* **10**, 171–172 (2020).
9. Arriagada, N. B., Bowman, D. M., Palmer, A. J. & Johnston, F. H. Climate change, wildfires, heatwaves and health impacts in australia. In *Extreme Weather Events and Human Health*, 99–116 (Springer, 2020).
10. Giglio, L., Schroeder, W. & Justice, C. O. The collection 6 MODIS active fire detection algorithm and fire products. *Remote Sensing of Environment* **178**, 31–41. URL <http://www.sciencedirect.com/science/article/pii/S0034425716300827>.
11. Binney, J. J., Dowrick, N. J., Fisher, A. J. & Newman, M. E. *The theory of critical phenomena: an introduction to the renormalization group* (Oxford University Press, 1992).

12. McKenzie, D. & Kennedy, M. C. Power laws reveal phase transitions in landscape controls of fire regimes. *Nature Communications* **3**, 1–6 (2012).
13. Scheffer, M. *Critical transitions in nature and society* (Princeton University Press, 2020).
14. Drossel, B. & Schwabl, F. Self-organized critical forest-fire model. *Physical review letters* **69**, 1629 (1992).
15. Palmieri, L. & Jensen, H. J. The forest fire model: the subtleties of criticality and scale invariance. *Frontiers in Physics* **8**, 257 (2020).
16. Scheffer, M. *et al.* Early-warning signals for critical transitions. *Nature* **461**, 53–59 (2009).
17. van Nes, E. H. *et al.* What do you mean, ‘tipping point’? *Trends in ecology & evolution* **31**, 902–904 (2016).
18. Rocha, J. C., Peterson, G., Bodin, Ö. & Levin, S. Cascading regime shifts within and across scales. *Science* **362**, 1379–1383 (2018).
19. Wuyts, B., Champneys, A. R. & House, J. I. Amazonian forest-savanna bistability and human impact. *Nature Communications* **8**, 1–12 (2017).
20. Lovejoy, T. E. & Nobre, C. Amazon tipping point (2018).
21. Scanlon, T. M., Caylor, K. K., Levin, S. A. & Rodriguez-Iturbe, I. Positive feedbacks promote power-law clustering of kalahari vegetation. *Nature* **449**, 209–212 (2007).
22. Taubert, F. *et al.* Global patterns of tropical forest fragmentation. *Nature* **554**, 519–522 (2018).
23. Saravia, L. A., Doyle, S. & Bond-Lamberty, B. Power laws and critical fragmentation in global forests. *Scientific Reports* **8**, 17766. URL <https://doi.org/10.1038/s41598-018-36120-w>.
24. Clauset, A., Shalizi, C. R. & Newman, M. E. Power-law distributions in empirical data. *SIAM review* **51**, 661–703 (2009).
25. Marsili, M., Mastromatteo, I. & Roudi, Y. On sampling and modeling complex systems. *Journal of Statistical Mechanics: Theory and Experiment* **2013**, P09003 (2013).

26. Gerlach, M. & Altmann, E. G. Testing statistical laws in complex systems. *Physical review letters* **122**, 168301 (2019).
27. Wilson, K. G. The renormalization group and critical phenomena. *Reviews of Modern Physics* **55**, 583 (1983).
28. Loreto, V., Pietronero, L., Vespignani, A. & Zapperi, S. Renormalization group approach to the critical behavior of the forest-fire model. *Physical review letters* **75**, 465 (1995).
29. Goldenfeld, N. *Lectures on phase transitions and the renormalization group* (CRC Press, 2018).
30. Jona-Lasinio, G. The renormalization group: A probabilistic view. *Il Nuovo Cimento B (1971-1996)* **26**, 99–119 (1975).
31. De Domenico, M., Granell, C., Porter, M. A. & Arenas, A. The physics of spreading processes in multilayer networks. *Nature Physics* **12**, 901–906 (2016).
32. Kivelä, M. *et al.* Multilayer networks. *Journal of complex networks* **2**, 203–271 (2014).
33. De Domenico, M., Nicosia, V., Arenas, A. & Latora, V. Structural reducibility of multilayer networks. *Nature communications* **6**, 1–9 (2015).
34. Gillespie, D. T. Exact stochastic simulation of coupled chemical reactions. *The journal of physical chemistry* **81**, 2340–2361 (1977).
35. Marro, J. & Dickman, R. *Nonequilibrium phase transitions in lattice models* (Cambridge University Press, 2005).
36. Martín, P. V., Domínguez-García, V. & Muñoz, M. A. Intermittent percolation and the scale-free distribution of vegetation clusters. *New Journal of Physics* **22**, 083014 (2020).
37. Keeley, J. E., Pausas, J. G., Rundel, P. W., Bond, W. J. & Bradstock, R. A. Fire as an evolutionary pressure shaping plant traits. *Trends in Plant Science* **16**, 406–411 (2011).
38. Jyoteeshkumar reddy, P., Perkins-Kirkpatrick, S. E. & Sharples, J. J. Intensifying australian heatwave trends and their sensitivity to observational data. *Earth's Future* **9**, e2020EF001924 (2021).

39. Steel, Z. L. *et al.* Ecological resilience and vegetation transition in the face of two successive large wildfires. *Journal of Ecology* (2021).
40. Nolan, R. H. *et al.* Limits to post-fire vegetation recovery under climate change. *Plant, cell & environment* (2021).
41. Fairman, T. A. *et al.* Too much, too soon? A review of the effects of increasing wildfire frequency on tree mortality and regeneration in temperate eucalypt forests. *International Journal of Wildland Fire* **25**, 831–848 (2015).
42. de L. Dantas, V., Batalha, M. A. & Pausas, J. G. Fire drives functional thresholds on the savanna–forest transition. *Ecology* **94**, 2454–2463 (2013).
43. Oliveras, I. & Malhi, Y. Many shades of green: the dynamic tropical forest–savannah transition zones. *Philosophical Transactions of the Royal Society B: Biological Sciences* **371**, 20150308 (2016).
44. Biodiversity in flames. *Nature Ecology & Evolution* **4**, 171–171 (2020).
45. Dinerstein, E. *et al.* An Ecoregion-Based Approach to Protecting Half the Terrestrial Realm. *BioScience* **67**, 534–545 (2017).
46. R Core Team. *R: A Language and Environment for Statistical Computing*. R Foundation for Statistical Computing, Vienna, Austria (2021). URL <https://www.R-project.org/>.
47. Pikovsky, A., Rosenblum, M. & Kurths, J. Synchronization: a universal concept in nonlinear science (2002).
48. Bhattacharjee, S. M. & Seno, F. A measure of data collapse for scaling. *Journal of Physics A: Mathematical and General* **34**, 6375 (2001).
49. Stauffer, D. & Aharony, A. *Introduction to percolation theory* (CRC press, 2018).